Middle East versus Saharan dust extinction-to-backscatter ratios

A. Nisantzi[1], R. E. Mamouri[1], A. Ansmann[2], G. L. Schuster[3], and D. G. Hadjimitsis[1]

[1]Cyprus University of Technology, Dep. of Civil Engineering and Geomatics, Limassol, Cyprus
[2]Leibniz Institute for Tropospheric Research, Leipzig, Germany
[3]NASA Langley Research Center, Hampton, Virgina, USA

Abstract. Four years (2010–2013) of observations with polarization lidar and sun/sky photometer at the combined European Aerosol Research Lidar Network (EARLINET) and Aerosol Robotic Network (AERONET) site of Limassol (34.7° N, 33° E), Cyprus, were used to compare extinction-to-backscatter ratios (lidar ratios) for desert dust from Middle East deserts and the Sahara. In an earlier article, we analyzed one case only and found comparably low lidar ratios <40 sr for Middle East dust. The complex data analysis scheme is presented. The quality of the retrieval is checked within a case study by comparing the results with respective Raman lidar solutions for particle backscatter, extinction, and lidar ratio. The applied combined lidar/photometer retrievals corroborate recent findings regarding the difference between Middle East and Saharan desert dust lidar ratios. We found values from 43–65 sr with a mean (± standard deviation) of 53±6 sr for Saharan dust and from 33–48 sr with a mean of 41±4 sr for Middle East dust for the wavelength of 532 nm. The presented data analysis, however, also demonstrates the difficulties in identifying the optical properties of dust even during outbreak situations in the presence of complex aerosol mixtures of desert dust, marine particles, fire smoke, and anthropogenic haze.

1 Introduction

The particle extinction-to-backscatter ratio or lidar ratio S is an important quantity in the description of atmospheric aerosols with lidar (Müller et al., 2007; Burton et al., 2012; Groß et al., 2013) and a key input parameter in the retrieval of vertical profiles of the particle extinction coefficient from measurements with elastic backscatter lidars (Fernald, 1984; Ansmann, 2006) such as the spaceborne Cloud Aerosol Lidar with Orthogonal Polarization (CALIOP) (Omar et al.,

2009). Profiles of the particle extinction coefficient throughout the troposphere and stratosphere belong to the basic input data sets in atmospheric modeling of the direct aerosol effect on climate. Dust-related extinction coefficient profiles are also used to estimate ice nuclei concentrations up to cirrus level (Mamouri and Ansmann, 2014b). Present and upcoming spaceborne lidar activities (Winker et al., 2009; Stoffelen et al., 2005; Ansmann et al., 2007; Illingworth et al., 2015) need lidar-ratio information for all relevant aerosol types such as urban haze, biomass burning smoke, desert dust and marine particles in key areas of climate relevance for a consistent interpretation of the space-lidar-derived aerosol and cloud products.

Because desert dust is one of the major atmospheric aerosol components and the Sahara and the deserts in the Middle East (Syria, Jordan, Israel, Iraq, Arabian peninsula) are among the major dust sources of the world, the investigation and quantification of the optical properties including the lidar ratio of Saharan and Middle East dust is an important contribution to atmospheric and climate research. Recent Aerosol Robotic Network (AERONET) sunphotometer-based studies of Schuster et al. (2012) and combined observations with polarization lidar and sun/sky photometer by Mamouri et al. (2013) suggest that lidar ratios of Middle East dust are significantly lower (35–45 sr) than the ones for Saharan dust (45–60 sr). The reason seems to be that the illite concentration in dust particles decreases from values around 80 % in western Saharan regions to less than 5 % in the dust particles in eastern Saharan and Middle East desert regions (Schuster et al., 2012). As a consequence the real part of the refractive index decreases from 1.55 for Arabian dust to 1.45 for western Saharan dust for the 500–550 nm wavelength range and the lidar ratio drops from values around 60 sr for western Saharan dust to values around or below 40 sr for Middle East dust.

More studies are needed to corroborate these findings. For this reason we analyzed the full 2010-2013 lidar/photometer

---

data set available for the Limassol station regarding Middle East and Saharan dust outbreaks. Mamouri et al. (2013) demonstrated that a polarization lidar is a basic requirement for a trustworthy retrieval of dust optical properties. The polarization-lidar approach allows us to distinguish dust and non-dust contributions to the overall particle optical properties and to extract the dust–related lidar ratio information from the total aerosol backscatter and extinction properties. There is almost no continental site in the northern hemisphere which is not affected by omnipresent anthropogenic particles so that lidar-derived extinction-to-backscatter ratios, even when directly determined by means of the Raman-lidar or the High Spectral Resolution Lidar method, are not trustworthy as long as measurements of the depolarization ratio (showing, e.g., values of >0.3 in the dust layers at 532 nm) are not available. After long-range transport across the oceans, significant mixing with marine particles can never be excluded so that again direct dust lidar-ratio observations need to be interpreted with care when depolarization ratio measurements are missing or show values clearly below 0.3 at 532 nm.

There are already a lot of studies on Saharan dust lidar ratios mostly based on Raman lidar observations (Mattis et al., 2002; Amiridis et al., 2005; Mona et al., 2006; Papayannis et al., 2008; Esselborn et al., 2009; Tesche et al., 2009b, 2011; Groß et al., 2011; Preißler et al., 2013). For heavy dust loads the lidar ratio was typically in the range of 45–60 sr for western Saharan dust sources. Most lidars did not have a polarization sensitive channel for aerosol type separation so that it remains unknown to what extent the retrieval of dust optical properties is biased by the presence of non-dust particles. Respective efforts regarding Middle East dust are not available.

High quality dust lidar ratio observations are also required to support photometer-based retrievals, because sun photometers do not provide direct observations of 180° scattering, the lidar ratio cannot be measured and is obtained from modeling. A spheroidal particle shape model is used together with the observed spectral aerosol optical thickness (AOT) and sky radiance measurements to simulate the particle backscatter coefficient and the lidar ratio (Dubovik et al., 2006). The particle shape model assumes that the irregularly shaped dust particles are ideal spheroids. Because column-integrated particle information is measured when using sun photometers, lidar ratios for lofted dust layers above a polluted boundary layer (PBL) cannot be distinguished.

The assumption of a spheroidal shape of the dust particles may cause uncertainties in the column dust lidar ratios of the order of 10 % or even more (Müller et al., 2010; Gasteiger et al., 2011; Wagner et al., 2013). However, Schuster et al. (2012) emphasized the strong influence of the real part of the refractive index on the particle optical properties. The real part dictates the scattering efficiency and has a strong impact on the computation of the extinction and backscatter coefficients. Any aerosol contribution (anthro-

pogenic fine-mode haze) to the column aerosol observation was found to decrease the column-integrated real part derived with AERONET and to increase the derived column lidar ratio. Schuster et al. (2012) thus contrasted polluted dust for which the fine-mode volume fraction FVF is > 0.05 and pure dust scenarios with FVF < 0.05.

Another source of uncertainty in AERONET lidar-ratio retrievals arise from the fact that the presence of particles with radius $>15\,\mu$m is ignored in the complex data analysis which is partly based on inversion methods for which a the size spectrum of the particles have to be known a priori. AERONET measurement in the source regions, at heavy dust conditions, or even after long-range transport, but within 30 hours after emission, may be affected by the presence of giant dust particles (Ansmann et al., 2010).

In this article, we summarize our four-year lidar-ratio observations and present the dust lidar-ratio findings of 17 Middle East and 32 Saharan dust outbreaks. A first lidar-based study of a strong Middle East desert dust outbreak was presented by Mamouri et al. (2013) to highlight the comparably low lidar ratios (34-39 sr) for Arabian dust. The Limassol lidar station at the island of Cyprus in the eastern Mediterranean Sea is unique because it is the only site of the European Aerosol Research Lidar Network (EARLINET) which is influenced by a statistically significant number (5–7) of Middle East dust outbreaks each year as well as by numerous Saharan dust outbreaks ($> 10\,\mathrm{year}^{-1}$). However, the eastern Mediterranean and the adjacent southwestern Asian and northern African areas are also highly polluted, which strongly complicates the data analysis. As already observed during the United Arab Emirates Unified Aerosol Experiment (UAE[2]) campaign (Reid et al., 2008), the Southwest Asian region is one of the most difficult environments of the world regarding characterizing, modeling and monitoring of the atmospheric state. Frequent dust storms, high anthropogenic aerosol levels, and complex air flow pattern dominate the region. This is reflected in our observations, too.

Simultaneous EARLINET lidar and AERONET sun photometer observations were conducted at Limassol almost daily over the four-year period from May 2010 to December 2013. One of the goals is to cover the overpass times of polar orbiting satellites. Therefore the observations were usually taken between 7 and 13 UTC (9 - 15 local time). Nighttime (Raman lidar) observation were only occasionally performed. The data analysis is thus based on the 532 nm elastic backscatter signals and makes use of methodology recently introduced by Mamouri et al. (2013).

In Sect. 2, the lidar and sun/sky photometer instruments are briefly described. Section 3 presents the method applied to derive dust-related lidar ratios from elastic-backscatter signal profiles. The results are discussed in Sect. 4.1 and 4.2. The reliability of our methodology for the retrieval of dust-related lidar ratios, outlined in Sect. 3, is checked by means of direct Saharan dust lidar-ratio observation by applying the Raman lidar method (Mattis et al., 2002) during a

major Saharan dust storm (Sect. 4.3). In Sect. 5, we compare a limit number of lidar ratio observations with results derived from the AERONET sun photometer measurements alone (Schuster et al., 2012). Summarizing and concluding remarks are presented in Sect. 6.

2 Instrumentation

The remote sensing station of the Cyprus University of Technology (CUT) at Limassol (34.7° N, 33° E, 50 m a.s.l.) is equipped with an EARLINET lidar (Mamouri et al., 2013) and AERONET sun/sky photometer (CUT–TEPAK site, Limassol, Cyprus, http://aeronet.gsfc.nasa.gov) (Holben et al., 1998) and is located about 150 km south of Turkey and 250 km west of Syria.

The laser transmits linearly polarized laser pulses at 532 and 1064 nm, and detects the parallel and cross-polarized signal components at 532 nm. Calibration of the polarization channels is performed by rotating the box with the polarization sensitive channels following the methodology of Freudenthaler et al. (2009). Further measurement channels collect lidar return signals at 607 nm (nitrogen Raman channel) and 1064 nm (elastic backscatter). The full overlap of the laser beam with the receiver field of view of the 20 cm Cassegrain telescope is obtained at heights around 300 m a.s.l. and therefore in most cases within the shallow planetary boundary layer (PBL) reaching up to 350–500 m height. The basic temporal and spatial signal resolution, with which the raw signals are stored, is 50 s and 7.5 m, respectively.

The lidar system started performing systematic measurements in May 2010 as a 532 nm elastic-backscatter lidar. An hardware upgrade was realized in mid 2012 by integrating a 607 nm Raman channel. In order to provide homogeneous lidar data during the study period (May 2010 - December 2013) we used the vertical profiles of the 532 nm backscatter signals, only. Raman–lidar retrievals are only available at nighttime and only for the EARLINET measurement times (Monday and Thursday evenings). The Raman-lidar observation on 23 May 2013 was used to validate our lidar-ratio approach in the case of a strong Saharan dust outbreak with almost pure dust above 2.5 km height emitted in the central part of the Saharan desert.

In this paper, we will make mainly use of the determined particle backscatter coefficient and the particle depolarization ratio at 532 nm. The range-corrected signal at 1064 nm was used only to better illustrate the evolution of dust outbreaks in time-height displays (color plot in section 4.3). The retrieval products are computed from cloud-screened data sets, averaged over almost one hour and vertically smoothed with window lengths of 45 m (up to 2.5 km height), 60 m (up to 4 km height), and 90 m (above 4 km height). All data files showing low-level cloud contamination were removed before signal averaging.

Further information of the lidar, the methods applied to analyze the data, the products, and basic retrieval uncertainties can be found in Mamouri et al. (2013) and Mamouri and Ansmann (2014a). Details to the determination of the basic volume depolarization ratio profile are given by Nisantzi et al. (2014).

The CUT AERONET sun photometer provides AOT measurements at eight wavelengths from 339 to 1638 nm. It also provides retrievals of column-integrated particle size distributions, complex refractive index, and the number percentage of spherical particles (Dubovik and King, 2000). This is sufficient information to compute the column lidar ratio S_A (Schuster et al., 2012). From the particle size distribution the fine-mode volume fraction FVF is obtained. We further use the Ångström exponent AE (Ångström, 1964), determined from the spectral AOT distribution, and the fine mode fraction FMF (fraction of fine–mode AOT to total AOT) (O'Neill et al., 2003).

Additionally, during the yearly CIMEL calibration period and/or in case of technical problems, we used auxiliary a hand-held sun photometer (MICROTOPS II, solar light Company, USA) to obtain aerosol optical properties in five channels at 440, 500, 675, 870, 936 nm. To assure high accuracy the sun photometer is mounted in a tripod.

Our study includes a careful investigation of the air mass origin and long-range aerosol transport by means of backward trajectory analysis. The HYSPLIT (HYbrid Single-Particle Lagrangian Integrated Trajectory) model was used for this purpose. Access is provided via the NOAA ARL READY Website (http://www.arl.noaa.gov/HYSPLIT.php). HYSPLIT is described in detail by Draxler and Hess (1997, 1998), and Draxler (1999).

3 Data analysis procedure

The data analysis is based on simultaneous observations with polarization lidar and sun/sky photometer (daytime measurements) and follows the procedure outlined in Mamouri et al. (2013). For the correction of Rayleigh backscattering and extinction contributions to the observed signals we calculated the air molecule optical properties by assuming standard atmospheric conditions adjusted to actual surface conditions regarding temperature and pressure. The results in terms of particle backscatter coefficients differ by no more than a few percent (typically by 1 %) from calculation with temperature and pressure profiles taken from numerical weather prediction model outputs.

The following data analysis comprises ten steps. The products include the profiles of the particle backscatter coefficient separately for dust and non-dust aerosol components, the free tropospheric (FT) column dust and non-dust lidar ratios, and dust and non-dust-related particle optical depths of the lofted outbreak plumes. These ten steps are as follows:

1. We computed the profile of the particle backscatter coefficient with Eq. (2) in Mamouri et al. (2013) with the 532 nm AOT from the AERONET observations as a constraint. The 532 nm AOT follows from the measured 500 nm AOT combined with the 440-675 nm Ångström exponent. The conventional two-layer Fernald data analysis (Fernald, 1984; Ansmann, 2006; Mamouri et al., 2013) is applied. Layer 1 is the PBL reaching up to 350–500 m height. Layer 2 extends from the top of the PBL to the top of the lofted FT aerosol layer. By assuming a lidar ratio for the PBL of $S_{\mathrm{PBL}} = 25$–$35\,\mathrm{sr}$, we obtain the particle lidar ratio S_{T} for the entire tropospheric column and S_{FT} for the free tropospheric column. The PBL over the coastal city contains a mixture of marine particles showing a lidar ratio of about 20 sr (Groß et al., 2011) and urban haze with lidar ratios of about 50 sr (Müller et al., 2007). S_{PBL} values around 30 sr are typical for aerosol mixtures of anthropogenic haze and marine particles (Franke et al., 2001). The PBL AOT contribution is usually about 0.02-0.03, and thus <10-15% of the total AOT during dust outbreaks.

2. The particle linear depolarization ratio is calculated from the volume linear depolarization ratio by means of the particle backscatter coefficient profile (Freudenthaler et al., 2009; Tesche et al., 2009b).

3. HYSPLIT backward trajectory analysis together with the profiles of the particle depolarization ratio is used to identify cases with long-range transport of desert dust from the Middle East deserts or from northern Africa (Sahara region). 20–30 Middle East dust outbreaks of different strength crossed Cyprus during the four years under study. More than 50 cases of Saharan dust long-range transport were identified. For each case, we run the HYSPLIT model with respect to the height of the layers observed over Limassol to identify the source region(s) for the observed aerosol. Even observations with passive satellite sensors and estimated PBL heights over the potential source regions were taken into account in the final decision and identification of contributing aerosol sources.

4. From the total set of dust outbreaks we considered for further analysis (in Sect. 4) only cases in which the particle linear depolarization ratio exceeded 0.15 in the free troposphere and this for a height range of at least 500 m. In this way, we obtained 17 Middle East dust cases and 32 Saharan dust cases for our dust lidar-ratio investigations. A comparably low depolarization ratio threshold had to be selected to avoid the omission of too many dust layers. Pure dust layers are rare over Cyprus. Furthermore, fine–mode-dominated dust layers may show a likewise low depolarization ratio close to 0.15 (Mamouri and Ansmann, 2014a), but should be included in our data set.

5. In the next step, we calculated the geometrical properties of the remaining dust-containing layers (bottom and top heights). The height range for which the particle linear depolarization ratio is > 0.15 in the free troposphere represents the FT dust layer. Figure 1 shows base and top heights of all considered dust layers. The base of the FT dust layers frequently coincided with the top of the PBL. The PBL top height was determined from the lidar profiles. The first minimum of the first derivative of the lidar signal normalized to the calculated backscatter signal from atmospheric molecules was taken in most cases as PBL top height (Flamant et al., 1997). However, during dust outbreaks with dust layer base at PBL top, this method did not work. The PBL top was then usually indicated by a clear change in the signal strength as well as in the depolarization ratio. The depolarization ratio was often enhanced in the PBL, compared to a value around 2-3% as expected for a mixture of marine particles and urban haze. The presence of dust in the PBL does not affect the assumed lidar ratio S_{PBL} much, because this PBL lidar ratio is still dominated by the marine-urban aerosol mixture. The lidar ratios for urban haze and desert dust are not very different so that the additional presence of desert dust may have increased S_{PBL} towards 35 sr. We took this into account in the uncertainty analysis below. The top of the dust layers often reached to heights of 4–8 km a.s.l. This is in agreement with the spaceborne CALIOP lidar study presented by Liu et al. (2008).

6. For each case, the layer-mean linear particle depolarization ratio and the corresponding SD, indicating the variability of the values from base to top within the layer, was computed. Figure 2 provides an overview of the obtained layer-mean particle linear depolarization ratios. In most cases, the mean depolarization ratio was in the range from 0.17 to 0.28, and indicate aerosol mixtures with dust contributions to particle backscattering of 50–90 % according to Fig. 1 of Tesche et al. (2011).

7. By using the height profiles of the particle depolarization ratio and the particle backscatter coefficient we determine the dust and non-dust backscatter coefficient profiles (Tesche et al., 2009a) and, based on these profiles, we calculated the FT dust and non-dust column backscatter values (as given in Eq. (4) in Mamouri et al. (2013)). In this approach, we assumed a particle linear depolarization ratio of 0.05 for non–dust particles and 0.31 for dust particles so that depolarization ratios < 0.05 and > 0.31 indicate a pure non-dust aerosol and a pure dust aerosol, respectively (Freudenthaler et al., 2009; Tesche et al., 2009a; Groß et al., 2011). Mixtures

are indicated by depolarization ratios from > 0.05 to < 0.31.

8. In the retrieval of the FT dust lidar ratio $S_{\mathrm{FT,d}}$ (in the next step 9), we need to assume a FT column lidar-ratio $S_{\mathrm{FT,s}}$ for (spherical) non-dust particles. For this, we carefully inspected the backward trajectories. If the air masses only crossed maritime areas before arriving at Limassol, we selected $S_{\mathrm{FT,s}}$ from 25–30 sr. This is for example the case when dust layers are advected from the Sahara over the polluted Mediterranean Sea to Cyprus on the most direct way. An example is shown in Sect. 4.1 (30 September 2010). If the dust-laden air masses crossed continental (industrialized, urbanized) areas at low heights then we selected 50–55 sr for $S_{\mathrm{FT,s}}$. Sect. 4.1 also contains an example for this scenario (17 May 2011). If satellite imagery (Nisantzi et al., 2014) indicated that the air masses crossed even regions with biomass burning, we selected $S_{\mathrm{FT,s}}$ of 65–70 sr in a few cases. This step of the retrieval introduces a large uncertainty. It was found that the impact of the $S_{\mathrm{FT,s}}$ assumption is low for FT dust backscatter fractions $D_\beta > 0.8$, and high for dust backscatter fractions D_β around 0.5, which was frequently the case. The FT column dust backscatter fraction D_β is defined as the ratio of column-integrated dust backscatter coefficient to column-integrated total (dust and non-dust) particle backscatter coefficient for the free troposphere:

$$D_\beta = \frac{\int_{R_1}^{R_2} \beta_{\mathrm{FT,d}}(z)\,\mathrm{d}z}{\int_{R_1}^{R_2} \beta_{\mathrm{FT}}(z)\,\mathrm{d}z}. \tag{1}$$

9. By using the selected $S_{\mathrm{FT,s}}$ value, we estimated finally $S_{\mathrm{FT,d}}$, after Eq. (4) in Mamouri et al. (2013). Rearrangement of this equation yields

$$S_{\mathrm{FT,d}} = \frac{S_{\mathrm{FT}} - (1 - D_\beta) S_{\mathrm{FT,s}}}{D_\beta}. \tag{2}$$

10. Finally we compute (a) the FT aerosol particle optical thickness $\mathrm{AOT_{FT}}$ from the particle backscatter coefficient profile and the column FT lidar ratio S_{FT}, (b) the FT dust and non-dust particle optical thicknesses $\mathrm{AOT_{FT,d}}$ and $\mathrm{AOT_{FT,s}}$ from the FT dust and non-dust backscatter coefficient profiles and the respective column lidar ratios $S_{\mathrm{FT,d}}$ and $S_{\mathrm{FT,s}}$, and (c) we estimated the dust fraction DF,

$$DF = \frac{\tau_{\mathrm{FT,d}}}{\tau_{\mathrm{T}}} \tag{3}$$

with the free-tropospheric dust AOT $\tau_{\mathrm{FT,d}}$ and the tropospheric AOT τ_{T} as measured with the AERONET sun photometer.

3.1 Retrieval uncertainties

As outlined in Mamouri et al. (2013), the uncertainty in $S_{\mathrm{FT,d}}$ is almost completely a function of the uncertainties in the assumed PBL lidar ratio S_{PBL} and the free tropospheric non-dust aerosol lidar ratio $S_{\mathrm{FT,s}}$. By varying each of the two input lidar ratios by ± 10 sr (around the assumed values), we estimated the mean uncertainty for each case and each of the two input parameters. In this way, we determined the mean uncertainties for both input lidar ratios S_{PBL} and $S_{\mathrm{FT,s}}$ for all 49 cases. The uncertainty in $S_{\mathrm{FT,d}}$ for each case is then calculated from the square root of the quadratic sum of the S_{PBL} and $S_{\mathrm{FT,s}}$ error contributions plus a respective uncertainty term resulting from a 10% uncertainty in the separation of the dust and spherical particle components with the depolarization–ratio technique. These uncertainties are shown as error bars in the last figure of Sect. 4.2. This error computation yields typical uncertainties of 13–19% in the dust lidar ratios.

In this error analysis, we ignore minor contributions by signal noise, uncertainties in the required Rayleigh extinction and backscatter calculations, and in the particle reference value, which may increase the overall relative uncertainty by further 5–10 %. We also ignore a minor impact of a few percent by the assumption of the backscatter profile slope in the lowermost 300 m (region of incomplete laser-beam receiver-field-of-view overlap, see respective particle backscatter profile in several figures of Sect. 4). Here, we used the same assumption (linear decrease of particle backscattering from the surface to 300 m height by a factor of 2) as in Mamouri et al. (2013).

4 Results

We begin the discussion of our four-year observations with two measurement examples to explain the different steps of the data analysis in detail (Sect. 4.1). An overview of all measurements is then presented in Sect. 4.2. During a few major dust outbreaks, the Raman lidar method (Mattis et al., 2002) could be applied so that desert-dust lidar ratios could directly be determined in the dense dust layers, in which the particle depolarization ratio showed values around 0.3 at 532 nm. In this way, an in-depth proof of our entire analysis concept as described in Sect. 3 could be performed. Such a case is discussed in Sect. 4.3.

4.1 Case studies of 30 September 2010 (Saharan dust) and 17 May 2013 (Middle East dust)

All observational cases considered in our study were conducted at times from 07:00–13:00 UTC. For all cases sun photometer observations (AERONET or with hand-held MICROTOPS II sun photometer) are available. Figure 3 shows two cases with pronounced dust layers above the PBL. According to the backward trajectories in Fig. 4 a Saharan dust

layer and a Middle East desert dust plume were monitored. In both cases, the FT AOT of 0.16 and 0.87 strongly contributed to the total tropospheric AOT of 0.22 and 0.91, respectively.

In the first step, we obtain the height profile of the particle backscatter coefficient (Mamouri et al., 2013) and the FT lidar ratio S_{FT}. The 532 nm particle optical depth measured with the sun photometer is used as constraint. A boundary-layer lidar ratio of 30 sr is assumed. It is further assumed that the backscatter coefficient linerally decreases by a factor of 2 from 300 m above ground down to the surface as mentioned above. In step 2, we determine the particle depolarization ratio, and subsequently, the backscatter contributions by non-dust and dust particles (step 7, example is shown in Sect. 4.3 and in Mamouri et al. (2013) and Mamouri and Ansmann (2014a)), and the backscatter fraction D_β (step 8). In step 9, we obtain the FT dust lidar ratio $S_{FT,d}$ with Eq. (2). Here, we need to assume the non-dust lidar ratio $S_{FT,s}$. We selected 25 sr (Fig. 3 left, assuming a slightly polluted marine aerosol besides desert dust) and 55 sr (Fig. 3 right, assuming mainly anthropogenic particles in the FT aerosol mixture besides the dust). Finally, we are able to estimate all optical depth contributions of the different aerosol components, and the dust fraction DF (step 10).

The dust backscatter fractions of $D_\beta = 0.84$ and 0.98 indicate that dust clearly dominated the optical properties in the free troposphere. The layer mean particle depolarization ratios were high with values of 0.26 (Saharan dust) and 0.30 (Middle East dust). DF was 0.72 (Saharan dust) and 0.96 (Middle East dust).

Note that even at 4.5-5 km height dust is detected over Cyprus on 30 September 2010, although the backward trajectory arriving at 4.5 km height is permanently above 4.5 km height. This indicates that dust plumes over northern Africa typically reach heights up to 4-6 km above ground during the summer halfyear (Tesche et al., 2009b). Because all Saharan trajectories indicate a direct air mass transport from the Sahara towards Cyprus (across the polluted Mediterranean Sea) and therefore a very low influence of European haze on the aerosol mixture, we selected a non-dust lidar ratio for free tropospheric aerosols of $S_{FT,s} = 25$ sr which may indicate the impact of marine particles as well as anthropogenic aerosols over northern Africa. The resulting dust lidar ratio $S_{FT,d}$ was comparably low with a value of 47 sr. However, this value may be representative for the northeastern Saharan region in agreement with the findings of Schuster et al. (2012) who noticed a steady decrease of the lidar ratio from values of 50–60 sr for western Saharan dust towards 40–45 sr for Middle East dust.

In contrast to the Saharan dust case, a large AOT of 0.91 was observed during a Middle East dust event on 17 May 2011. An almost pure dust plume reached from 500 m to 5 km height. According to the backward trajectories (see Fig. 4, lower panel) all air masses which crossed Cyprus between 2–5 km height were close to the ground over the Mid-

dle East region. This explains the high dust load at all heights up to 5 km in this case. Non-dust aerosol contributions to the observed aerosol mixture were related to European haze, marine particles over the Mediterranean, and anthropogenic aerosols over the southwestern Asian states according to the backward trajectories. As a consequence, we selected a FT non-dust lidar ratio of $S_{FT,s} = 55$ sr. However, at these dust-dominating conditions, this estimate (and the related uncertainties) has almost no influence on the result in terms of dust lidar ratio $S_{FT,d}$, which was 43 sr and thus close to the values found by Schuster et al. (2012) and Mamouri et al. (2013). Unfortunately we have no AERONET-derived lidar ratio for these two days because of problems with the sun photometer. Only hand-held MICROTOPS sun photometer observations of the AOT could be performed on these days.

4.2 Statistics: Middle East vs. Saharan dust lidar ratios

The initial goal of the study was to provide lidar ratios for pronounced desert dust layers with dominant backscattering by mineral dust particles. However, as mentioned above, such conditions are rare. Dust layers mixed with anthropogenic aerosol and marine particles prevail over Cyprus (see Table 1). Almost pure dust layers are observed when $D_\beta > 0.8$ (see Eq. (1)). For these conditions, our retrieval delivers the most reliable results and the relative uncertainty in the dust lidar ratio is low with values down to 10 %. In Figs. 5 and 6 overviews of our data analysis for all 17 major Middle East and 32 Saharan dust outbreaks are presented. Figure 5 shows the Middle East dust lidar ratios. For the observed six cases with dust backscatter fractions of $D_\beta > 0.8$ and corresponding layer mean particle depolarization ratios of > 0.25 (April 2011 to May 2012), $S_{FT,d}$ ranges from 42–46 sr. For the less dust-dominated 11 cases with D_β from 0.22–0.7 most dust lidar ratios were found between $S_{FT,d} = 35$ and 40 sr. Here the uncertainty in the $S_{FT,d}$ values introduced by the non-dust lidar ratio assumptions is high (of the order of 10–15 sr). The mean Middle East dust lidar ratio of all 17 cases is 41.1 ± 4.3 sr.

Figure 6 shows the retrieval results for the Saharan dust outbreaks. For the found six cases with $D_\beta > 0.8$ we obtain lidar ratios from 47–65 sr with four values in the range from 55–60 sr. We found 14 cases (out of the 32 Saharan dust cases) with layer mean particle depolarization ratios > 0.25. For these cases, the lidar ratios accumulate in the range from 50–55 sr. In contrast to the Middle East dust events, we assumed low FT non-dust lidar ratios $S_{FT,s}$ because the air masses have a comparably long distance across the Mediterranean Sea towards Cyprus and the anthropogenic aerosol level over North Africa is lower than over the southwestern Asian region. Most FT dust backscatter fractions D_β and Saharan DF values were in the range from 0.4–0.8 and 0.4–0.7, respectively, which clearly indicates that non-dust aerosol types always contributed to the observed particle backscatter and extinction properties. The mean value of the 32 Saha-

ran dust lidar ratios is 52.7 ± 6.1 sr. This lidar ratio is close to the value of 55 sr found by Tesche et al. (2009b) for pure Saharan dust cases.

Figure 7 provides an impression of the uncertainty in the lidar-ratio retrieval. Realistic uncertainties in the most important input parameters are simulated to produce the shown error bars. Although the error bars show uncertainties of the order of 5-12 sr and the corresponding mean SDs (indicated as dashed horizontal lines) in Fig. 7 are large, a difference between the Saharan and Middle East dust lidar ratios is visible. According to the mean values (horizontal solid lines) the Middle East dust lidar ratios are, on average, lower by 12 sr than the Saharan dust lidar ratios.

Table 1 provides additional insight into the aerosol mixing characteristics of the evaluated aerosol scenarios. There were only minor differences between the listed values for Middle East and Saharan dust outbreaks. Comparably high Ångström exponents were measured over Cyprus with the AERONET sun photometer during the dust events. These column observations always include the more polluted lowest parts of the atmosphere over the island. Pure dust extinction (and AOT) usually causes an Ånsgtröm exponents of 0.0–0.2 (Tesche et al., 2009b, 2011). Also the fine mode fraction, FMF, is high compared to values of 0.1–0.25 for strong dust outbreaks (Mamouri and Ansmann, 2014a). The dust AOT fraction DF and the dust backscatter fractions D_β are, on average, much lower than for clearly dust-dominating cases with values of >0.8. Table 1 also contains statistics on the derived Saharan and Middle East dust lidar ratios, separately for $D_\beta > 0.8$ and when considering the full data sets.

It is worth to note that values in Table 1 are in agreement with a study of Eck et al. (2008). During the UAE[2] campaign, performed in the United Arab Emirates and the adjacent Arabian Gulf region in August–September 2004, they found, on average, Ångström exponents of 0.5–0.77 (440–870 nm spectrum) for the 14 AERONET stations with slightly higher values for coastal and island sites compared to stations in the center of continental desert regions. Mean 500 nm FMF values ranged from 0.2–0.8. These values were mainly caused by strong fine-mode particle sources from petroleum extraction and processing facilities. Only during rather strong dust events (over the desert stations) the Ångström exponent dropped to typical dust values of 0.22–0.31 and the FMF were in the range from 0.24–0.29. According to Reid et al. (2008) and Eck et al. (2008) it was hard to observe pure dust optical properties, even in desert-dominated areas.

4.3 Case study of 23 May 2013: Raman lidar observation

We checked the quality of the results obtained with the method described in Sect. 3 for cases where we could include the Raman signals in the aerosol analysis. The Raman lidar technique makes use of both, the elastic backscatter sig-

nals at 532 nm and the nitrogen Raman signals measured at 607 nm wavelength, and provides height profiles of the particle backscatter and extinction coefficients and thus a direct vertically resolved observation of the desert dust lidar ratio in pronounced dust layers (Mattis et al., 2002), if the depolarization ratio is around 0.3 at 532 nm which is the case here. In the following, we compare the findings obtained with the Raman lidar method and with our approach (Sect. 3) which is based on elastic-backscatter signals only.

Figure 8 shows the arrival of the thick Saharan dust plume over Limassol in the morning of 23 May 2013. According to the backward trajectories arriving above 2 km height at 19:00 UTC (see Fig. 9), the lofted Saharan dust layer between 2.5 and 5.5 km height originated from the central parts of the Sahara. Over about 4–5 days, dust could be collected by the air masses before traveling to Cyprus within 1–2 days. The layer below 2 km height contained a mixture of Saharan dust, European haze, and maritime particles according to the red backward trajectories for the arrival height of 1750 m.

An almost constant aerosol layering was observed above 2000 m from 17:30–20:50 UTC (see Fig. 8, second observational period after 17:30 UTC). We used this period for a detailed inspection of the optical properties of the Saharan dust plume by applying the Raman lidar method. Figure 10 shows the mean profiles of the 532 nm particle backscatter and extinction coefficients for the 17:47–20:50 UTC time period, and the respective height profile of the lidar ratio. The 532 nm dust-related optical depth was close to 0.38. As can be seen, in agreement with the backward trajectories, the lidar ratio shows typical Saharan dust values between 50–60 sr around the center of the dust layer at 3.5–4.0 km height. In the layer with European haze between 1.0 and 1.5 km height, the lidar ratio is close to 50 sr, and decreases to values below 30 sr at heights < 1.0 km. As mentioned, values of 25–35 sr are typical for a mixture of anthropogenic and maritime particles (Franke et al., 2001).

In Fig. 11, the products obtained with our retrieval scheme (Sect. 3) are presented. Because after sunset no AERONET data are available, we used the lidar-derived total particle AOT of 0.45 as a constraint in step 1 (see Sect. 3). The AOT was determined from the extinction profile in Fig. 10 (left panel) down to 1 km height and the backscatter profile below 1 km multiplied by a lidar ratio of 30 sr for the lowermost 1 km of the troposphere. The laser-beam RFOV overlap function prohibits a trustworthy extinction profiling by means of the Raman-lidar method below about 500-700 m. As a result of step 1, we obtain the column lidar ratio of $S_{FT} = 57$ sr for the free troposphere and of $S_T = 55.8$ sr for the total tropospheric column. This value is close to the AERONET-derived total tropospheric lidar ratio of $S_A = 58$ sr obtained from the afternoon sun photometer observations (13:00–14:00 UTC). The tropospheric AOT was 0.33 at 500 nm to that time, measured during periods without cirrus clouds.

In step 2 of the data analysis, the particle linear depolar-

ization ratio shown in Fig. 11 is computed. By means of the profiles of the particle backscatter coefficient and depolarization ratio the profile of the dust backscatter coefficient can then be calculated (step 7, red profile in Fig. 11) so that the column dust backscatter value for the free troposphere and the respective dust fraction D_β can be calculated (given as number in Fig. 11). The profiles for the particle backscatter coefficient in Figs. 10 and 11 slightly differ because of different methods (Raman-lidar versus Fernald method) used in the two figures and the different signal smoothing lengths (750 m versus 45-90 m).

To obtain the dust-related lidar ratio $S_{FT,d}$ (steps 8 and 9), we use Eq. (2). Disregarding the clear evidence that we observed a pronounced dust layer above 2 km on 23 May 2013, we split the troposphere into the PBL (reaching up to 500 m) and the free troposphere (from 500–7000 m height). This was generally done for all cases of the four-year period discussed below. We assumed a PBL lidar ratio of $S_{PBL} = 30\,sr$ and a non-dust lidar ratio $S_{FT,s} = 50\,sr$ for the free troposphere accounting for the anthropogenic particles mainly confined to the layer from 500–2000 m height.

The FT column dust backscatter value D_β of 0.834 in Fig. 11 indicates a dominating dust contribution to the measured optical effects. DF was also 0.83. The FT column dust lidar ratio $S_{FT,d}$ was found to be close to 58 sr and thus close to the dust layer mean lidar ratio of 56 sr derived from the Raman lidar observations (see Fig. 10). The influence of uncertainties in the assumed PBL lidar ratio S_{PBL} on the retrieved dust lidar ratio $S_{FT,d}$ is low because the AOT of the PBL is less than 10 % of the total AOT. The uncertainty introduced by an error in the FT non-dust lidar ratio $S_{FT,s}$ of 10 sr results in an uncertainty of $< 5\,sr$ in the derived $S_{FT,d}$ value. Figures 10 and 11 corroborate that our retrieval scheme presented in Sect. 3 allows us to determine dust-related lidar ratios with good accuracy.

5   Comparison with AERONET observations of dust lidar ratios

Only a limited number of published lidar-ratio studies is available for comparison. As mentioned in the introduction, most lidar studies did not take the non-dust particle contribution to the observed mixed-aerosol lidar ratios into consideration. Cattrall et al. (2005) and Schuster et al. (2012) extensively discuss Saharan and Middle East dust lidar ratios based on AERONET observations. As also mentioned, these column-integrated measurements include the contribution of PBL aerosols (marine particles, local anthropogenic haze, local road and soil dust) and are frequently affected by long-range transport of non-dust aerosol (fire smoke, lofted marine particles, anthropogenic aerosol).

During events with a strong dust load with AOTs exceeding 0.4, Schuster et al. (2012) found mean values for the desert dust lidar ratio at 532 nm wavelength of 56.4 sr

(over North African AERONET sites), 57.8 sr (Non-Sahel African stations), 55.1 sr (African Sahel sites), and 47.2 sr (AERONET stations in Middle East desert areas) for dust-dominated summer months from May to September in the years of 2006 to 2009. During very strong dust events (pure dust cases) with fine-mode volume fraction FVF < 0.05 and thus negligible impact of anthropogenic particles on the computations the lidar ratios were on average about 10 % lower.

Cattrall et al. (2005) analyzed the main dust periods from 1994 to 2004 over eastern Asian, Middle East, and North African AERONET stations and found mean values of 39–41 sr for several Middle East sites and 35–38 sr for Saharan sites for the wavelength of 550 nm. Cattrall et al. (2005) used an older, less sophisticated AERONET inversion technique which may explain the differences with respect to the results of Schuster et al. (2012).

Figure 12 provides a comparison between lidar-based (S_T) and AERONET-based (S_A) retrieval results for the total tropospheric column. Six Middle East dust events and 14 Saharan dust cases are available for this comparison. Only this limited number of AERONET data could be analyzed. Most of the data are quality-assured AERONET data (level 2.0). However, the majority of AERONET observations were performed at AOTs clearly below 0.4 so that the uncertainty is high (Dubovik et al., 2000; Schuster et al., 2012). None of the shown cases passed the pure-dust criteria (FVF < 0.05). As mentioned in the introduction, the problem with fine-mode haze is that these particles lower the overall refractive index. The fine mode is more optically efficient than the coarse mode, and increases the lidar ratio when compared to pure-dust scenarios. The impact of anthropogenic aerosol is less dominant in the case of lidar retrievals (Fernald data analysis) at 532 nm wavelength. Coarse mode particles widely control the measured optical effects during dust outbreak situations. This is consistent with the results in Fig. 12. The tropospheric column lidar ratios retrieved from the AERONET observations are in most of the selected dust outbreak cases larger than the lidar-derived lidar ratios. If we further keep in mind that the dust lidar ratio $S_{FT,d}$ is, on average, 8±4 sr higher than the tropospheric lidar ratio S_T for the considered 14 Saharan dust scenes according to the lidar data analysis and lower by about 3±2 sr for the six Middle East dust cases, one may conclude that it is almost impossible to retrieve reliable dust lidar ratios at sites in the Mediterranean region from AERONET observations, or mode general, outside the deserts.

6   Conclusions

A study of dust particle lidar ratios for two major desert dust regions and sources for atmospheric dust has been presented. The particle lidar ratio is an important quantity in the description of atmospheric aerosols and aerosol mixtures in the framework of aerosol typing efforts. It is a key in-

put parameter in the retrieval of height profiles of climate relevant particle extinction coefficient, derived from widely used elastic backscatter lidars including the spaceborne lidar CALIOP. Present and upcoming spaceborne lidar activities need lidar-ratio information for all relevant aerosol types for a consistent interpretation of the space-lidar-derived aerosol and cloud products around the globe.

We found a significant difference with mean values of 53 ± 6 and $41 \pm 4\,sr$ for Saharan and Middle East desert dust, respectively, which is in good agreement with literature values. A recently introduced polarization lidar technique (Mamouri et al., 2013) for the extraction of dust lidar ratio information from elastic-backscatter lidar observations was applied to the four-year Cyprus data set.

The study corroborates earlier findings that desert dust plumes contain a mixture of desert dust and a variety of other aerosol components (marine particles, fire smoke, anthropogenic haze). Lofted pure desert dust plumes are more the exception than the rule. From this point of view it is a rather difficult effort to select the optimum lidar ratio in the analysis of CALIOP observations over deserts and adjacent regions. The measurement of the particle depolarization ratio is demanding in order to be able to identify and quantify the dust contribution to the aerosol load and more generally for a high-quality aerosol typing.

References

Amiridis, V., Balis, D. S., Kazadzis, S., Bais, A., Giannakaki, E., Papayannis, A., and Zerefos, C.: Four-year aerosol observations with a Raman lidar at Thessaloniki, Greece, in the framework of European Aerosol Research Lidar Network (EARLINET), J. Geophys. Res., 110, D21203, doi:10.1029/2005JD006190, 2005.

Amiridis, V., Wandinger, U., Marinou, E., Giannakaki, E., Tsekeri, A., Basart, S., Kazadzis, S., Gkikas, A., Taylor, M., Baldasano, J., and Ansmann, A.: Optimizing CALIPSO Saharan dust retrievals, Atmos. Chem. Phys., 13, 12089–12106, doi:10.5194/acp-13-12089-2013, 2013.

Ångström, A.: The parameters of atmospheric turbidity, Tellus, 16, 64–75, 1964.

Ansmann, A.: Ground-truth aerosol lidar observations: can the Klett solutions obtained from ground and space be equal for the same aerosol case?, Appl. Optics, 45, 3367–3371, 2006.

Ansmann, A., Wandinger, U., Le Rille, O., Lajas, D., and Straume, A. G.: Particle backscatter and extinction profiling with the spaceborne high-spectral-resolution Doppler lidar ALADIN: methodology and simulations, Appl. Opt, 46, 6606–6626, 2007.

Ansmann, A., Baars, H., Tesche, M., Müller, D., Althausen, D., Engelmann, R., Pauliquevis, T., and Artaxo, P.: Dust and smoke transport from Africa to South America: lidar profiling over Cape Verde and the Amazon rainforest, Geophys. Res. Lett., 36, L11802, doi:10.1029/2009GL037923, 2009.

Ansmann, A., Tesche, M., Groß, S., Freudenthaler; V., Seifert, P., Hiebsch, A., Schmidt, J., Wandinger, U., Mattis, I., Müller, D., and Wiegner, M.: The 16 April 2010 major volcanic ash plume over central Europe: EARLINET lidar and AERONET photometer observations at Leipzig and Munich, Germany, Geophys. Res. Lett., 37, L13810, doi:10.1029/2010GL043809, 2010.

Baars, H., Ansmann, A., Althausen, D., Engelmann, R., Artaxo, P., Pauliquevis, T., and Souza, R.: Further evidence for significant smoke transport from Africa to Amazonia, Geophys. Res. Lett., 38, L20802, doi:10.1029/2011GL049200, 2011.

Burton, S. P., Ferrare, R. A., Hostetler, C. A., Hair, J. W., Rogers, R. R., Obland, M. D., Butler, C. F., Cook, A. L., Harper, D. B., and Froyd, K. D.: Aerosol classification using airborne High Spectral Resolution Lidar measurements – methodology and examples, Atmos. Meas. Tech., 5, 73–98, doi:10.5194/amt-5-73-2012, 2012.

Cattrall, C., Reagan, J., Thome, K., and Dubovik, O.: Variability of aerosol and spectral lidar and backscatter and extinction ratios of key aerosol types derived from selected Aerosol Robotic Network locations, J. Geophys. Res., 110, D10S11, doi:10.1029/2004JD005124, 2005.

Draxler, R. R.: HYSPLIT4 User's Guide, NOAA Tech. Memo. ERL ARL-230, NOAA Air Resources Laboratory, Silver Spring, MD, 1999.

Draxler, R. R. and Hess, G. D.: Description of the HYSPLIT 4 Modeling System, NOAA Tech. Memo. ERL ARL–224, NOAA Air Resources Laboratory, Silver Spring, MD, 1997.

Draxler, R. R. and Hess, G. D.: An overview of the HYSPLIT 4 modeling system of trajectories, dispersion, and deposition, Aust. Meteorol. Mag., 47, 295–308, 1998.

Dubovik, O. and King, M.: A flexible inversion algorithm for retrieval of aerosol optical properties from Sun and sky radiance measurements, J. Geophys. Res., 105, 20673–20696, doi:10.1029/2000JD900282, 2000.

Dubovik, O., Smirnov, A., Holben, B. N., King, M. D., Kaufman, Y. J., Eck, T. F., and Slutsker, I.: Accuracy assessments of aerosol optical properties retrieved from Aerosol Robotic Network (AERONET) Sun and sky radiance measurements, J. Geophys. Res., 105, 9791–9806, doi:10.1029/2000JD900040, 2000.

Dubovik, O., Sinyuk, A., Lapyonok, T., Holben, B. N., Mishchenko, M., Yang, P., Eck, T. F., Voltne, H., Munoz, O., Veihelmann, B., Van der Zande, W., J., Leon, J.-F., Sorokin, M., and Slutsker, I.: Application of spheroid models to account for aerosol particle nonsphericity in remote sensing of desert dust, J. Geophys. Res., 111, D11208, doi:10.1029/2005JD006619, 2006.

Eck, T. F., Holben, B. N., Reid, J. S., Sinyuk, A., Dubovik, O., Smirnov, A., Giles, D., O'Neill, N. T., Tsay, S.-C., Ji, Q., Al Mandoos, A., Ramzan Khan, M., Reid, E. A., Schafer, J. S., Sorokine, M., Newcomb, W., and Slutsker, I.: Spatial and temporal variability of column-integrated aerosol op-

tical properties in the southern Arabian Gulf and United Arab Emirates in summer, J. Geophys. Res., 113, D01204, doi:10.1029/2007JD008944, 2008.

Esselborn, M., Wirth, M., Fix, A., Weinzierl, B., Rasp, K., Tesche, M., and Petzold, A.: Spatial distribution and optical properties of Saharan dust observed by airborne high spectral resolution lidar during SAMUM 2006, Tellus B, 61, 131–143, doi:10.1111/j.1600-0889.2008.00394.x, 2009.

Fernald, F. G.: Analysis of atmospheric lidar observations: some comments, Appl. Optics, 23, 652–653, 1984.

Flamant, C., Pelon, J., Flamant, P. H., and Durand, P.: Lidar determination of the entrainment zone thickness at the top of the unstable marine atmospheric boundary-layer, Boundary- Layer Meteorol., 83, 247284, 1997.

Franke, K., Ansmann, A., Müller, D., Althausen, D., Wagner, F., and Scheele, R.: One-year observations of particle lidar ratio over the tropical Indian Ocean with Raman lidar, Geophys. Res. Lett., 28, 4559–4562, doi:10.1029/2001GL013671, 2001.

Freudenthaler, V., Esselborn, M., Wiegner, M., Heese, B., Tesche, M., Ansmann, A., Müller, D., Althausen, D., Wirth, M., Fix, A., Ehret, G., Knippertz, P., Toledano, C., Gasteiger, J., Garhammer, M., and Seefeldner, M.: Depolarization ratio profiling at several wavelengths in pure Saharan dust during SAMUM 2006, Tellus B, 61, 16579, doi:10.1111/j.1600-0889.2008.00396.x, 2009.

Gasteiger, J., Wiegner, M., Groß, S., Freudenthaler, V., Toledano, C., Tesche, M., and Kandler, K.: Modelling lidar-relevant optical properties of complex mineral dust aerosols, Tellus B, 63, 725–741, doi:10.1111/j.1600-0889.2011.00559.x, 2011.

Groß, S., Tesche, M., Freudenthaler, V., Toledano, C., Wiegner, M., Ansmann, A., Althausen, D., and Seefeldner, M.: Characterization of Saharan dust, marine aerosols and mixtures of biomass-burning aerosols and dust by means of multi-wavelength depolarization and Raman lidar measurements during SAMUM 2, Tellus B, 63, 706724, doi:10.1111/j.1600-0889.2011.00556.x, 2011.

Groß, S., Esselborn, M., Weinzierl, B., Wirth, M., Fix, A., and Petzold, A.: Aerosol classification by airborne high spectral resolution lidar observations, Atmos. Chem. Phys., 13, 2487–2505, doi:10.5194/acp-13-2487-2013, 2013.

Holben, B. N., Eck, T. F., Slutsker, I., Tanré, D., Buis, J. P., Setzer, A., Vermote, E., Reagan, J. A., Kaufman, Y. J., Nakajima, T., Lavenu, F., Jankowiak, I., and Smirnov, A.: AERONET – a federated instrument network and data archive for aerosol characterization, Remote Sens. Environ., 66, 1–16, 1998.

Illingworth, A. J., Barker, H. W., Beljaars, A., Ceccaldi, M., Chepfer, H., Clerbaux, N., Cole, J., Delanoe, J., Domenech, C., Donovan, D. P., Fukuda, S., Hirakata, M., Hogan, R. J., Huenerbein, A., Kollias, P., Kubota, T., Nakajima, T., Nakajima, T. Y., Nishizawa, T., Ohno, Y., Okamoto, H., Oki, R., Sato, K., Satoh, M., Shephard, M., Velazquez Blazquez, A., Wandinger, U., Wehr, T., and van Zadelhoff, G.-J.: The Earthcare Satellite: the next step forward in global measurements of clouds, aerosols, precipitation and radiation, B. Am. Meteorol. Soc., 96, doi:10.1175/BAMS-D-12-00227.1, in press, 2015.

Liu, D., Wang, Z., Liu, Z., Winker, D., and Trepte, C.: A height resolved global view of dust aerosols from the first year CALIPSO lidar measurements, J. Geophys. Res., 113, D16214, doi:10.1029/2007JD009776, 2008.

Mamouri, R. E. and Ansmann, A.: Fine and coarse dust separation with polarization lidar, Atmos. Meas. Tech., 7, 3717–3735, doi:10.5194/amt-7-3717-2014, 2014a.

Mamouri, R. E. and Ansmann, A.: Dust-related ice nuclei profiles from polarization lidar: methodology and case studies, Atmos. Chem. Phys. Discuss., 14, 25747–25786, doi:10.5194/acpd-14-25747-2014, 2014b.

Mamouri, R. E., Ansmann, A., Nisantzi, A., Kokkalis, P., Schwarz, A., and Hadjimitsis, D.: Low Arabian dust extinction-to-backscatter ratio, Geophys. Res. Lett., 40, 4762–4766, doi:10.1002/grl.50898, 2013.

Mattis, I., Ansmann, A., Müller, D., Wandinger, U., and Althausen, D.: Dual-wavelength Raman lidar observations of the extinction-to-backscatter ratio of Saharan dust, Geophys. Res. Lett., 29, 1306, doi:10.1029/2002GL014721, 2002.

Mona, L., Amodeo, A., Pandolfi, M., and Pappalardo, G.: Saharan dust intrusions in the Mediterranean area: three years of Raman lidar measurements, J. Geophys. Res., 111, D16203, doi:10.1029/2005JD006569, 2006.

Müller, D., Ansmann, A., Mattis, I., Tesche, M., Wandinger, U., Althausen, D., and Pisani, G.: Aerosol-type-dependent lidar ratios observed with Raman lidar, J. Geophys. Res., 112, D16202, doi:10.1029/2006JD008292, 2007.

Müller, D., Weinzierl, B., Petzold, A., Kandler, K., Ansmann, A., Müller, T., Tesche, M., Freudenthaler, V., Esselborn, M., Heese, B., Althausen, D., Schladitz, A., Otto, S., and Knippertz, P.: Mineral dust observed with AERONET Sun photometer, Raman lidar and in situ instruments during SAMUM 2006: shape-independent particle properties, J. Geophys. Res., 115, D11207, doi:10.1029/2009JD012523, 2010.

Nisantzi, A., Mamouri, R. E., Ansmann, A., and Hadjimitsis, D.: Injection of mineral dust into the free troposphere during fire events observed with polarization lidar at Limassol, Cyprus, Atmos. Chem. Phys., 14, 12155–12165, doi:10.5194/acp-14-12155-2014, 2014.

Omar, A. H., Winker, D. M., Kittaka, C., Vaughan, M. A., Liu, Z., Hu, Y., Trepte, C. R., Rogers, R. R., Ferrare, R. A., Lee, K.-P., Kuehn, R. E., and Hostetler, C. A.: The CALIPSO automated aerosol classification and lidar ratio selection algorithm, J. Atmos. Ocean. Tech., 26, 1994–2014, doi:10.1175/2009JTECHA1231.1, 2009.

O'Neill, N. T., Eck, T. F., Smirnov, A., Holben, B. N., and Thulasiraman, S.: Spectral discrimination of coarse and fine mode optical depth, J. Geophys. Res., 108, 4559, doi:10.1029/2002JD002975, 2003.

Papayannis, A., Amiridis, V., Mona, L., Tsaknakis, G., Balis, D., Bösenberg, J., Chaikovski, A., De Tomasi, F., Grigorov, I., Mattis, I., Mitev, V., Müller, D., Nickovic, S., Pérez, C., Pietruczuk, A., Pisani, G., Ravetta, F., Rizi, V., Sicard, M., Trickl, T., Wiegner, M., Gerding, M., Mamouri, R. E., D'Amico, G., and Pappalardo, G.: Systematic lidar observations of Saharan dust over Europe in the frame of EARLINET (2000–2002), J. Geophys. Res., 113, D10204, doi:10.1029/2007JD009028, 2008.

Preißler, J., Wagner, F., Guerrero-Rascado, J. L., and Silva, A. M.: Two years of free-tropospheric aerosol layers observed over Portugal by lidar, J. Geophys. Res.-Atmos., 118, 3676–3686, doi:10.1002/jgrd.50350, 2013.

Reid, J. S., Piketh, S. J., Walker, A. L., Burger, R. P., Ross, K. E.,

Westphal, D. L., Bruintjes, R. T., Holben, B. N., Hsu, C., Jensen, T. L., Kahn, R. A., Kuciauskas, A. P., Al Mandoo, A., Mangoosh, A., Miller, S. D., Porter, J. N., Reid, E. A., and Tsay, S.-C.: An overview of UAE2 flight operations: observations of summertime atmospheric thermodynamic and aerosol profiles of the southern Arabian Gulf, J. Geophys. Res., 113, D14213, doi:10.1029/2007JD009435, 2008.

Schuster, G. L., Vaughan, M., MacDonnell, D., Su, W., Winker, D., Dubovik, O., Lapyonok, T., and Trepte, C.: Comparison of CALIPSO aerosol optical depth retrievals to AERONET measurements, and a climatology for the lidar ratio of dust, Atmos. Chem. Phys., 12, 7431–7452, doi:10.5194/acp-12-7431-2012, 2012.

Stoffelen, A., Pailleux, J., Källén, E., Vaughan, J. M., Isaksen, L., Flamant, P., Wergen, W., Andersson, E., Schyberg, H., Culoma, A., Meynart, R., Endemann, M., and Ingmann, P.: The Atmospheric Dynamics Mission for global wind field measurements, B. Am. Meteorol. Soc., 86, 73–87, 2005.

Tesche, M., Ansmann, A., Müller, D., Althausen, D., Engelmann, R., Freudenthaler, V., and Groß, S.: Vertically resolved separation of dust and smoke over Cape Verde using multiwavelength Raman and polarization lidars during Saharan Mineral Dust Experiment 2008, J. Geophys. Res., 114, D13202, doi:10.1029/2009JD011862, 2009a.

Tesche, M., Ansmann, A., Müller, D., Althausen, D., Mattis, I., Heese, B., Freudenthaler, V., Wiegner, M., Eseelborn, M., Pisani, G., and Knippertz, P.: Vertical profiling of Saharan dust with Raman lidars and airborne HSRL in southern Morocco during SAMUM, Tellus B, 61, 144–164, doi:10.1111/j.1600-0889.2008.00390.x, 2009b.

Tesche, M., Groß, S., Ansmann, A., Müller, D., Althausen, D., Freudenthaler, V., and Esselborn, M.: Profiling of Saharan dust and biomass-burning smoke with multiwavelength polarization Raman lidar at Cape Verde, Tellus B, 63, 649–676, doi:10.1111/j.1600-0889.2011.00548.x, 2011.

Wagner, J., Ansmann, A., Wandinger, U., Seifert, P., Schwarz, A., Tesche, M., Chaikovsky, A., and Dubovik, O.: Evaluation of the Lidar/Radiometer Inversion Code (LIRIC) to determine microphysical properties of volcanic and desert dust, Atmos. Meas. Tech., 6, 1707–1724, doi:10.5194/amt-6-1707-2013, 2013.

Winker, D. M., Vaughan, M. A., Omar, A., Hu, Y., Powell, K. A., Liu, Z., Hunt, W. H., and Young, S. A.: Overview of the CALIPSO mission and CALIOP data processing algorithms, J. Atmos. Ocean. Tech., 26, 2310–2323, doi:10.1175/2009JTECHA1281.1, 2009.

Table 1. Desert dust layer statistics for 49 outbreaks (2010-2013): AERONET Ångström exponent (440-870 nm) and fine-mode fraction (ratio of 500 nm fine-mode AOT to AOT) for the tropospheric vertical column (T), and lidar-derived 532 nm dust AOT for the free troposphere (FT), dust fraction DF (Eq. (3)), the dust-layer mean particle linear depolarization ratio (532 nm), the backscatter fraction D_β (Eq. (1)), and the different lidar ratios (for Middle East, M. E., and Saharan dust). Mean value and standard deviation (SD) are given together with the range of observed values (from minimum to maximum value).

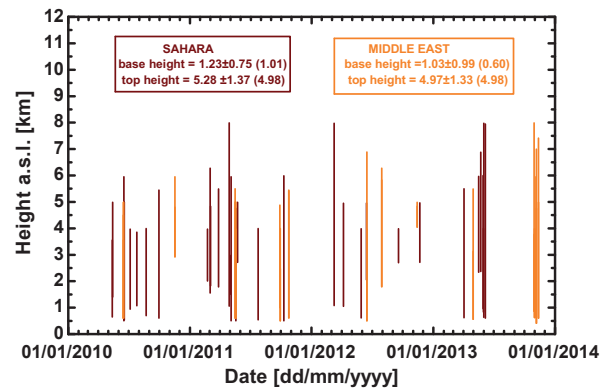| Parameter	Mean	SD	Min	Max
Ångström exponent (T)	0.75	0.42	0.04	1.63
Fine-mode fraction (T)	0.44	0.13	0.18	0.68
Dust AOT (FT)	0.20	0.20	0.04	1.15
Dust AOT fraction, DF (FT)	0.64	0.21	0.18	0.99
Depolarization ratio (FT)	0.24	0.04	0.17	0.35
Backscatt. fraction, D_β (FT)	0.62	0.22	0.19	0.99
Lidar ratio (M.E.), $D_\beta > 0.8$	44	1	43	46
Lidar ratio (M.E.)	41	4	33	48
Lidar ratio (Sah.), $D_\beta > 0.8$	56	6	47	65
Lidar ratio (Sah.)	53	6	43	65

Fig. 1. Lofted free–tropospheric desert dust layers (shown as vertical lines from bottom to top) observed between April 2010 and December 2013. The brown and orange vertical lines indicate 32 Saharan dust and 17 Middle East dust cases. The average bottom and top heights (plus the SD) of all detected dust layers are given as numbers. Median values are given in parentheses.
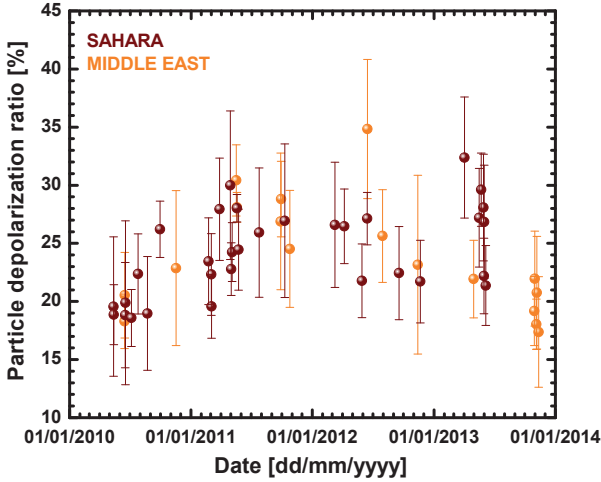
Fig. 2. Free-tropospheric dust layer mean particle linear depolarization ratio of all 32 Saharan dust (brown circles) and 17 Middle East dust cases (orange circles). The shown SDs (vertical bars) indicate the vertical variability within each layer in terms of the FT depolarization ratio.
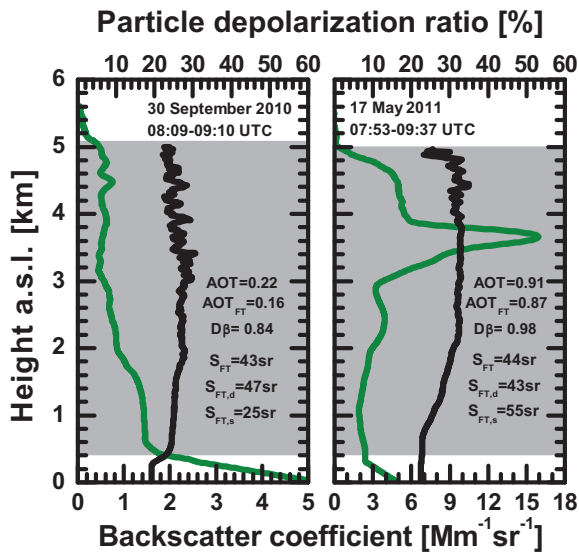

Fig. 3. 532 nm particle backscatter coefficient (green) and particle linear depolarization ratio (black) during a Saharan dust outbreak on 30 September 2010 (left) and a Middle East desert dust outbreak on 17 May 2011 (right). The gray-shaded areas indicate the identified main FT dust layers. Total tropospheric AOT, AOT_{FT} for the free troposphere, and several retrieved lidar ratios (S_{FT}, $S_{FT,d}$) are given as numbers. The dust fraction was DF=0.72 (30 September) and 0.96 (17 May). Assumed lidar ratios are $S_{PBL} = 30$ sr and $S_{FT,s} = 25$ sr (left panel) and 55 sr (right panel). The relative uncertainty in the backscatter coefficient and depolarization ratio is about 10% (Mamouri et al., 2013).
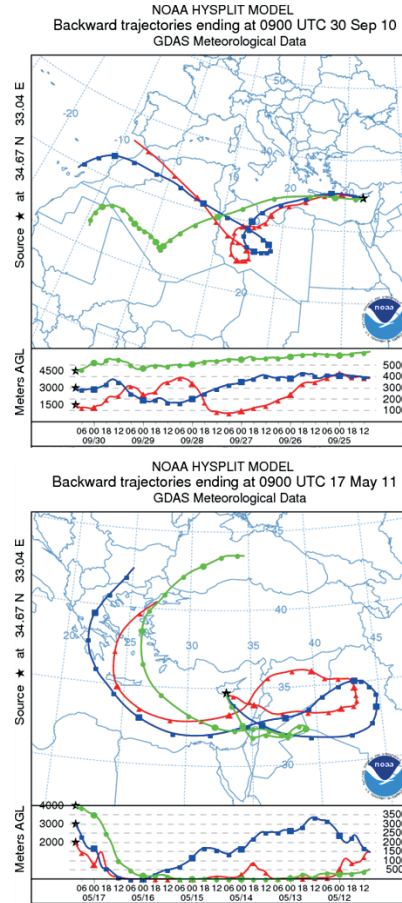
Fig. 4. Six-day HYSPLIT backward trajectories arriving at Limassol, Cyprus, at 1500 m (red, top) and 2000 m (red, bottom), 3000 m (blue), 4000 m (green, bottom), and 4500 m height (green, top) on 30 September 2010, 09:00 UTC (top) and 17 May 2011, 09:00 UTC (bottom).
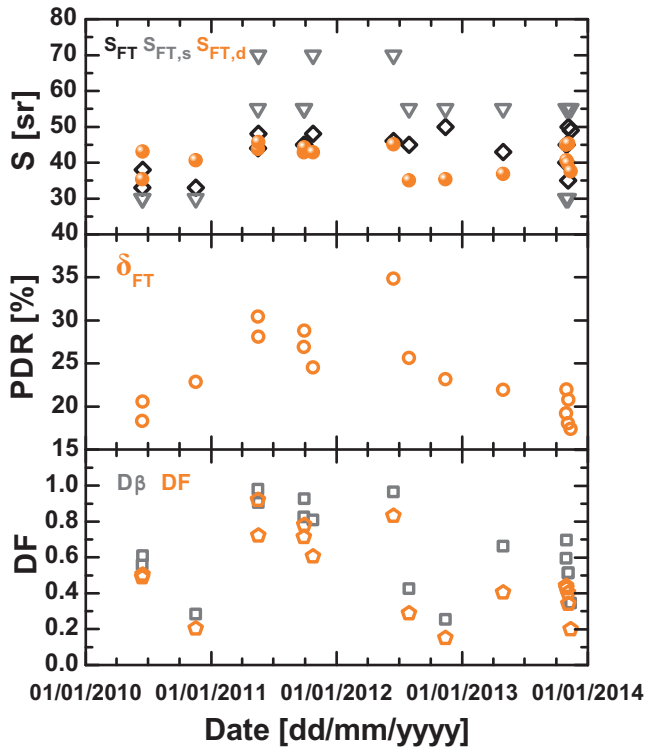
Fig. 5. (Top) Retrieved FT 532 nm lidar ratio S_{FT} (black diamonds), dust-related lidar ratio $S_{FT,d}$ (orange circles), and assumed non-dust lidar ratio $S_{FT,s}$ (gray triangles) for 17 Middle East dust outbreaks, (center) mean 532 nm particle linear depolarization ratio δ_{FT} for the entire free troposphere (above the PBL), and (bottom) 532 nm AOT dust fraction DF (orange pentagons, Eq. (3)), and FT dust backscatter fraction D_β (gray squares, Eq. (1)).
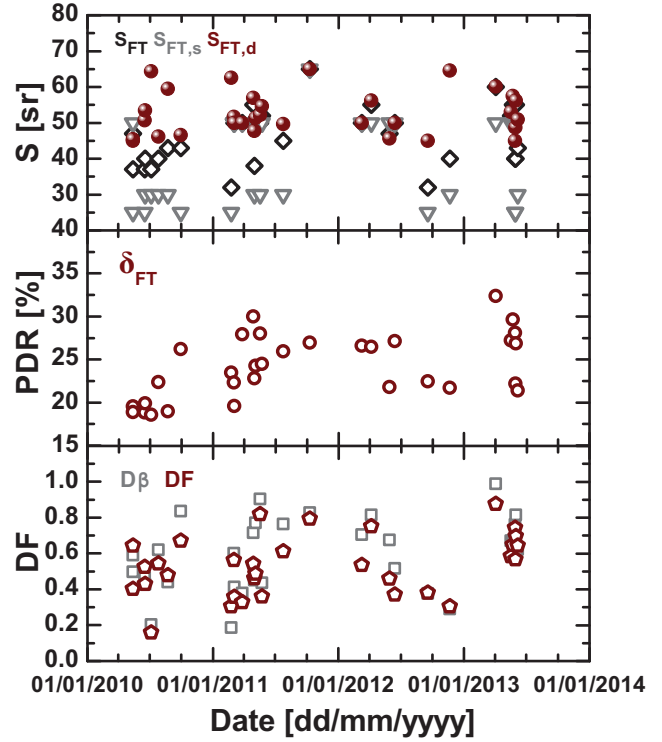

Fig. 6. Same as Fig. 5, except for Saharan dust outbreaks.
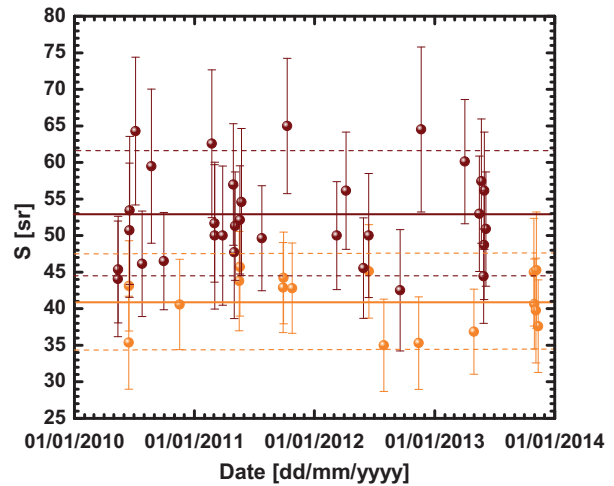
Fig. 7. Dust-related lidar ratio $S_{FT,d}$ as shown in Fig. 5 (orange, Middle East dust) and Fig. 6 (brown, Saharan dust) with error bars (standard deviation) caused by realistic ± 10 sr uncertainties in the lidar-ratio input parameters S_{PBL} and $S_{FT,s}$, and a 10% uncertainty in the separation of non-dust and dust backscatter coefficient. The solid and dashed (orange and brown) horizontal lines indicate the mean value of the 17 Middle East and 32 Saharan dust lidar ratios and the mean uncertainty (mean error bar length), respectively.
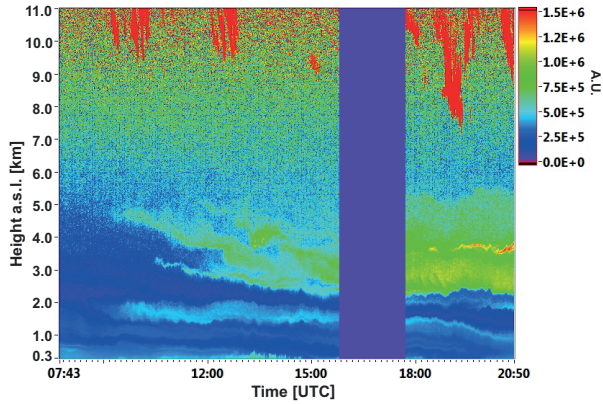
Fig. 8. Saharan dust outbreak advecting dust particles between 2 and 6 km height towards Limassol, Cyprus, on 23 May 2013. Range-corrected 1064 nm backscatter signals (in arbitrary units, A. U.) are shown. Red features above 7 km indicate ice clouds.
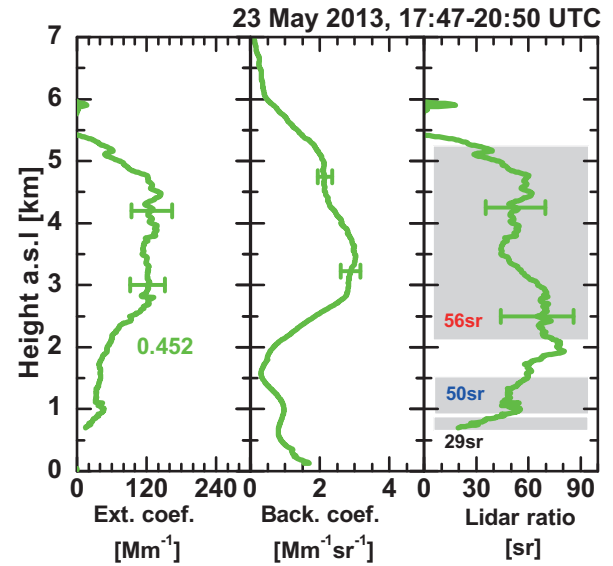

Fig. 10. Mean vertical profiles of the 532 nm particle extinction coefficient, backscatter coefficient, and lidar ratio for the observational period from 17:47–20:50 UTC on 23 May 2013. The Raman lidar method is applied. Vertical signal smoothing lengths of 600 m (below 1.1 km height), 1500 m (1.1–2.8 km height), and 2100 m (above 2.8 km height) are applied before computing the extinction coefficients and lidar ratios. The signal smoothing length is 750 m for the shown backscatter coefficient profile. Total AOT (given as number in the left panel) and layer mean values of the lidar ratio for the 0.7–0.85 km height layer (influenced by marine and local haze particles), the 0.86–1.5 km layer (influenced by European haze) and for the pure dust layer (2.1–5.2 km height range) are given as numbers. Error bars provide the uncertainty (standard deviation) by signal noise.
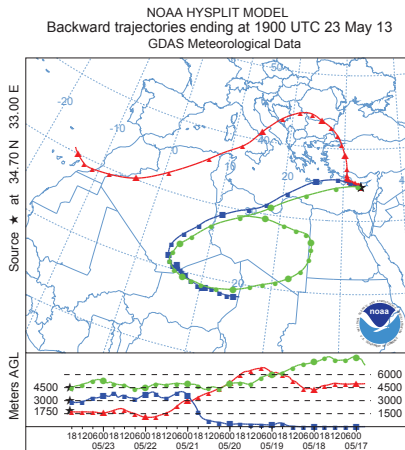

Fig. 9. Seven-day HYSPLIT backward trajectories arriving at Limassol, Cyprus, at 1750 m (red), 3000 m (blue), and 4500 m height (green) on 23 May 2013, 19:00 UTC.
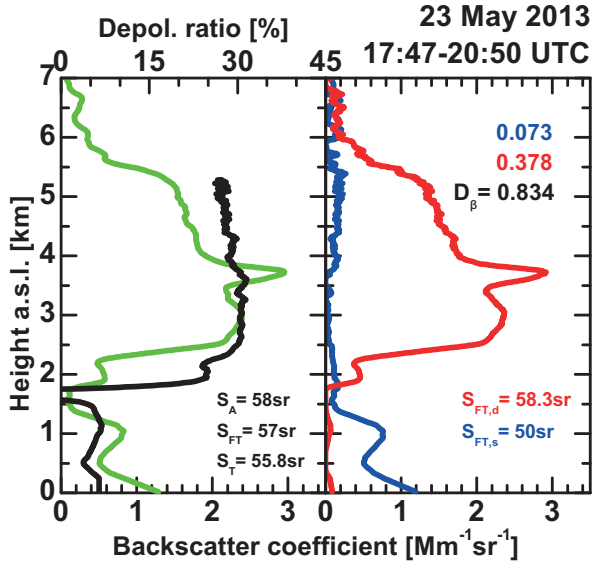
Fig. 11. Mean profiles (3 h average) of the 532 nm particle backscatter coefficient (left, green), particle linear depolarization ratio (left, black), dust backscatter coefficient (right, red), and non-dust particle backscatter coefficient (right, blue). The elastic-backscatter lidar method (explained in Sect. 3) is applied to the same observation as shown in Fig. 10. Retrieved column lidar ratios for the total troposphere (S_T), the free troposphere (S_{FT}), and derived from the AERONET data (S_A for the 13:00–14:00 UTC period) for the total tropospheric column after Schuster et al. (2012) are given as numbers in the left panel. S_{PBL} of 30 sr is assumed for the height range up to 500 m. The retrieved dust-related lidar ratio $S_{FT,d}$ and the assumed non-dust lidar ratio ($S_{FT,s}$) are given in the right panel together with the dust AOT (red number), non-dust AOT (blue number) for the total troposphere, and the FT dust backscatter fractions D_β (column dust backscatter to total particle backscatter in the free troposphere above 500 m height). Again, the relative uncertainty in the particle backscatter coefficient and depolarization ratio is 10%, and of the order of 20% for the dust-related backscatter coefficient (Mamouri et al., 2013).
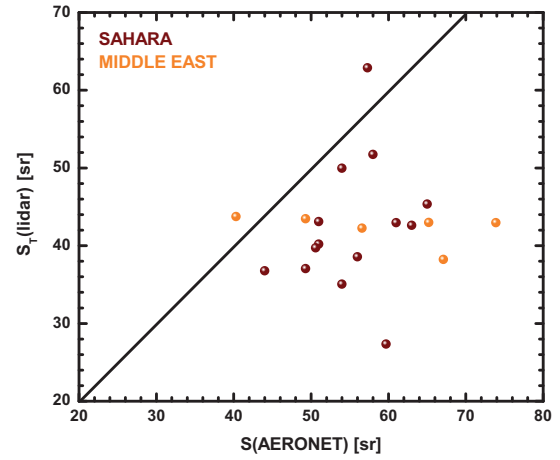

Fig. 12. Lidar-derived total tropospheric lidar ratio S_T vs. respective AERONET-derived lidar ratio S_A after Schuster et al. (2012). 14 Saharan dust events and 6 Middle East dust cases, observed over Limassol in the 2010-2013 period, could be analyzed. The solid line shows the 1 : 1 correlation line.